Received: 10 April 2019 | Revised: 9 January 2020 | Accepted: 27 January 2020

DOI: 10.1002/mrm.28218

FULL PAPER

Magnetic Resonance in Medicine

Analysis of EPI phase correction with low flip-angle excitation to reduce the required minimum TE: Application to whole-brain, submillimeter-resolution fMRI at 3 T

Seong Dae Yun[1] | **N. Jon Shah**[1,2,3,4]

[1]Institute of Neuroscience and Medicine 4, Medical Imaging Physics, Forschungszentrum Jülich, Jülich, Germany

[2]Institute of Neuroscience and Medicine 11, Molecular Neuroscience and Neuroimaging, JARA, Forschungszentrum Jülich, Jülich, Germany

[3]JARA-BRAIN-Translational Medicine, Aachen, Germany

[4]Department of Neurology, RWTH Aachen University, Aachen, Germany

Correspondence
N. Jon Shah, Institute of Neuroscience and Medicine 4, Forschungszentrum Jülich, 52425 Jülich, Germany.
Email: n.j.shah@fz-juelich.de

Funding information
International Research Training Group, Grant/Award Number: IRTG 2150

Purpose: Echo planar imaging is used widely for its imaging speed. However, its applications often suffer from ghost artifacts. In the community, an approach using three navigator echoes is used commonly for the artifact correction. Although this scheme is effective, as the matrix size increases for high-resolution imaging, the navigator echoes can contribute significantly to increasing the "required minimum TE." To overcome this issue, this work proposes the use of an alternative navigator echo scheme called the "TR-external" scheme.

Methods: The TR-external scheme reduces the required minimum TE by allocating an additional excitation loop for the navigator echoes before every main excitation loop. In this work, a detailed analysis on the TR-external scheme was performed to assess its performance in comparison to the standard scheme. Visual fMRI was performed to check the feasibility of using the TR-external scheme for detecting functional signals.

Results: The performance of the TR-external scheme was comparable with that of the standard scheme in terms of the SNR, elimination of ghost artifacts, and the BOLD detection. For a given matrix size (288 × 288), the TR-external scheme allowed a substantially shorter TE (5.94 ms) compared with the standard scheme, which resulted in a higher SNR. Furthermore, this feature enabled the submillimeter-resolution (0.73×0.73 mm^2) fMRI measurement with a favorable TE (35 ms) at 3 T. The fMRI results revealed that activated voxels are well localized along the cortical ribbon.

Conclusion: A TR-external scheme for EPI phase correction was implemented at 3 T. Its feasibility for submillimeter-resolution fMRI was successfully demonstrated.

KEYWORDS
EPI, fMRI, phase correction, short TE, submillimeter resolution, ultrahigh field

1 | INTRODUCTION

In spite of the fact that EPI is rather vulnerable to magnetic field inhomogeneities, it has been used widely in dynamic MR studies due to its relatively fast imaging speed. Consequently, EPI has been used to study various MR applications, such as DWI, perfusion imaging, and fMRI. EPI techniques have been steadily developed to improve performance and as a result, submillimetre spatial resolution is even possible in these EPI applications.[1-4]

Echo-planar-imaging applications often require a particular TE to achieve the desired image contrast. For fMRI applications, an optimal TE needs to be determined to derive strong BOLD contrasts at each field strength. Echo-planar imaging with high in-plane resolution requires a greater number of phase-encoding lines, which increases the minimum achievable TE. Thus, achieving the optimal TE for high in-plane resolution becomes increasingly difficult, in addition to other challenges such as maintaining sufficient SNR and reasonable level of T_2^* blurring and distortions. There have been many technical attempts to reduce the required minimum TE, such as combining in-plane acceleration techniques (eg, parallel imaging, partial Fourier, segmentation)[5-8] with EPI or non-Cartesian trajectories with sampling starting from the k-space center.[9] However, the use of acceleration techniques often induces additional drawbacks such as a substantial reduction of SNR (eg, by parallel imaging or partial Fourier) or an increased sensitivity for motion artifacts (eg, by segmentation). Furthermore, although the non-Cartesian trajectories are effective in achieving a shorter TE, they often suffer from imaging blurring caused by off-resonance effects. In this work, we were motivated to focus on Cartesian EPI and propose to use an alternative navigator echo scheme for EPI phase correction that does not yield any other significant disadvantages for reduction of the required minimum TE. This alternative scheme (called the "TR-external" scheme) has been described previously[10] but is not in widespread use, and its consequences for the SNR have not been explored in detail; this detailed description is the subject of the current manuscript.

In EPI, due to its zig-zag acquisition fashion, consequent gradient-sampling delays and technical limitations (eg, eddy currents, poor shimming), ghost artifacts are generated in reconstructed images. In the community, an approach that uses three non-phase-encoded navigator echoes is used commonly to correct the artifacts.[11] Although this approach is effective, as the matrix size increases for higher-resolution imaging, the navigator echoes play a significant part in contributing to the required minimum TE. The duration of each navigator echo is usually the same as that of the main EPI readout gradient lobe. Therefore, the TE increase caused by the navigator echoes is 3 times as large as the duration of the readout gradient lobe. As the matrix size increases, usually demanding a longer readout duration for each lobe, the length of the navigator echo readout increases concomitantly. Thus, the increase becomes larger as the matrix size increases for higher-resolution imaging. However, the TE increase can be effectively overcome by using the TR-external navigator echo scheme. This method allocates the navigator echoes in a separated low-flip-angle excitation loop, which precedes each main excitation and the corresponding EPI readout loop.[11,12] Here, because the navigator echoes are not an internal part of the main EPI acquisition loop, the navigator echoes have no effect on the increase of the required minimum TE, regardless of image matrix size. Therefore, the TR-external scheme can be used effectively in the applications that demand a shorter TE for their own purposes (eg, particular image contrast or a higher SNR). Alternatively, the capability of TE reduction in the TR-external scheme suggests its use to increase the matrix size for the given TE; a compromised approach may also be possible to achieve both the reduction of TE and an increase of the matrix size accordingly.

The TR-external scheme has not yet been analyzed in terms of the steady state, SNR, or optimal flip angle for the navigator echo. In this work, the steady-state equation of the TR-external scheme will be derived mathematically. Next, the performance of the method will be evaluated in terms of the strength of the transverse magnetization, temporal stability, and image SNR. Here, the optimal flip angle for the navigator echo will also be determined experimentally in relation to the robustness of the ghost removal. Finally, the capability of the TR-external scheme (ie, reduction of required minimum TE) is demonstrated with whole-brain (48 slices with 2.3-mm thickness) submillimeter-resolution (0.73×0.73 mm^2) fMRI. Here, for the given TE (35 ms), the maximum possible matrix size that can be provided by the TR-external scheme was 288×288. When the standard protocol is used instead, it is expected that a longer TE will be required for the same matrix size (288×288), or only a smaller matrix is possible for the same TE (35 ms).

2 | METHODS

2.1 | Echo-planar-image phase correction

Figure 1 shows two different navigator echo schemes for EPI phase correction: one with the "navigator echoes" in the same TR loop as the "main EPI readout" (standard; see Figure 1A) and the other with the "navigator echoes" in a separated TR loop (TR-external; see Figure 1B). The navigator echoes are acquired without phase prewinding to obtain the reference phase information of the even and odd lines. In the standard scheme, the navigator echoes are an internal part of the same TR loop as the main EPI readout; therefore, it can be seen that the navigator echoes contribute to the increase in the required minimum TE. Furthermore, to acquire navigator echoes without phase prewinding, the phase prewinding gradient (marked with black shading) needs to be located

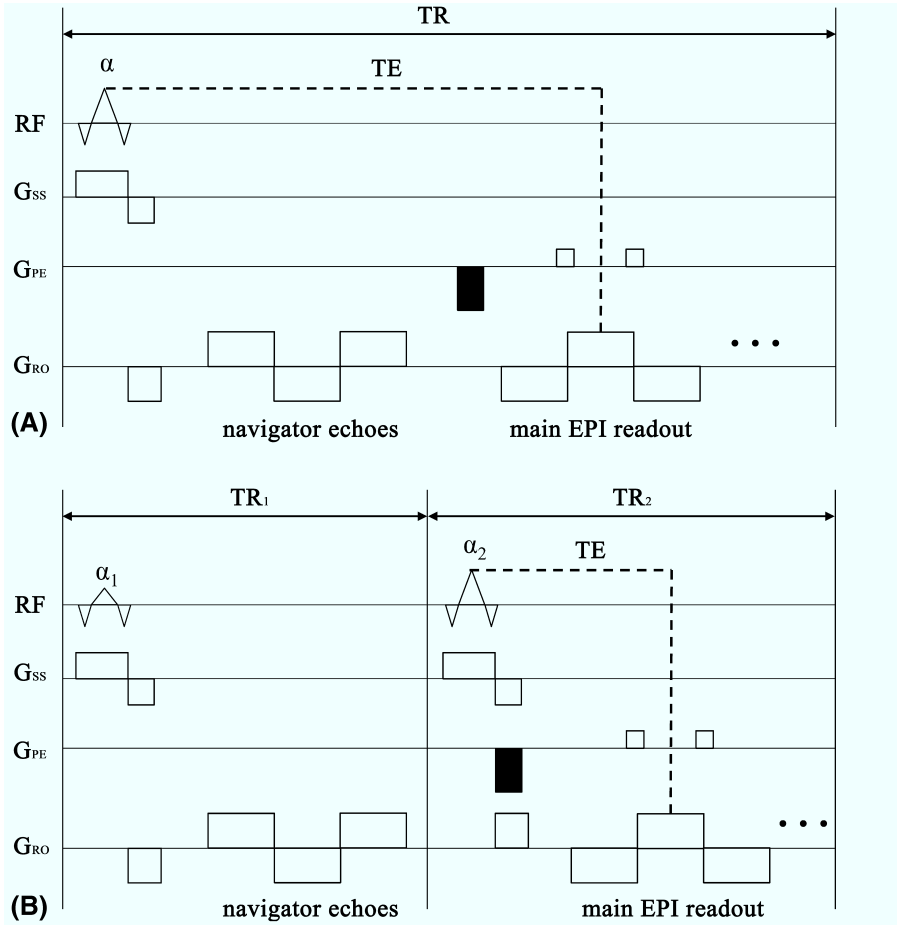

FIGURE 1 Schematic representation of the EPI sequences with the standard navigator echo scheme (A) and a "TR-external" navigator echo scheme (B). In the TR-external navigator echo scheme, the navigator echoes are located in a separated TR loop (TR_1), which precedes the main EPI TR loop (TR_2). The black-shaded gradients are phase prewinding gradients. In the TR-external scheme, the phase prewinding gradient can be located together with other encoding gradients as shown in (B)

after the navigator echoes. This constraint implies that the phase prewinding gradient cannot be applied together with other encoding gradients, such as the slice rephasing gradient and the readout dephasing gradient. Therefore, additional time is required for the phase prewinding gradient, which also contributes to the increase in the required minimum TE, although its amount is relatively small. For instance, without partial Fourier acceleration, when the matrix size is 64×64, 128×128, 192×192 and 256×256, typical durations for each phase prewinding gradient are 280, 440, 600 and 770 us, respectively.

Figure 1B depicts a TR-external scheme. In contrast to the standard scheme, this scheme requires an additional excitation pulse (flip angle of α_1) for the navigator echoes, which leads to a slight increase in total scanning time. However, the navigator echoes do not have any effect on the increase in the required minimum TE. Furthermore, it is even possible to place the phase prewinding gradient together with other encoding gradients; thus, an additional TE reduction is expected.

2.2 | Evolution of transverse magnetization: steady state

As described previously, the TR-external scheme requires two TR loops, each of which may have a different flip angle and TR. Here, to check whether the TR-external scheme reaches a steady state, the equation for the transverse magnetization was derived under the "steady-state incoherent" condition (ie, elimination of remaining transverse magnetization by spoiling).[13] The derived equation is given as follows:

$$M_{xy(n)}^{\text{ext}}(0^+) = M_{\text{eq}} \cdot \left[\begin{array}{l} (E_{\text{TR1}} \cdot \cos\alpha_1)^{n-1} \cdot (E_{\text{TR2}} \cdot \cos\alpha_2)^{n-2} \\ +(1-E_{\text{TR1}}) \cdot \dfrac{1-(E_{\text{TR1}} \cdot \cos\alpha_1 \cdot E_{\text{TR2}} \cdot \cos\alpha_2)^{n-1}}{1-(E_{\text{TR1}} \cdot \cos\alpha_1 \cdot E_{\text{TR2}} \cdot \cos\alpha_2)} \\ +(1-E_{\text{TR2}}) \cdot (E_{\text{TR1}} \cdot \cos\alpha_1) \cdot \dfrac{1-(E_{\text{TR1}} \cdot \cos\alpha_1 \cdot E_{\text{TR2}} \cdot \cos\alpha_2)^{n-1}}{1-(E_{\text{TR1}} \cdot \cos\alpha_1 \cdot E_{\text{TR2}} \cdot \cos\alpha_2)} \end{array} \right] \cdot \sin(\alpha_2) \quad (1)$$

$$\alpha_{2,\text{Ernst}} = \cos^{-1}\left(\cos\alpha_1 \cdot E_{\text{TR1}} \cdot E_{\text{TR2}}\right)$$

where $M_{xy(n)}^{ext}(0^+)$ and M_{eq} denote the transverse magnetization directly after the second TR loop excitation (α_2) and the magnetization at thermal equilibrium, respectively. Moreover, E_{TR1} and E_{TR2} indicate $\exp(-TR_1/T_1)$ and $\exp(-TR_2/T_1)$, respectively. Here, note that the Ernst angle ($\alpha_{2,\,Ernst}$) that maximizes the transverse magnetization in the main EPI loop also depends on the flip angle (α_1) and TR (TR_1) of the navigator echo loop.

For the standard scheme, well known from previous works, the equation is given as follows[14]:

$$M_{xy(n)}^{std}(0^+) = M_{eq} \cdot \left[\left(E_{TR} \cdot \cos\alpha\right)^{n-1} + \left(1 - E_{TR}\right) \cdot \frac{1 - \left(E_{TR} \cdot \cos\alpha\right)^{n-1}}{1 - \left(E_{TR} \cdot \cos\alpha\right)} \right] \cdot \sin(\alpha) \tag{2}$$

$$\alpha_{Ernst} = \cos^{-1}\left(E_{TR}\right)$$

where E_{TR} denotes $\exp(-TR/T_1)$.

It can be easily seen that these two equations eventually go to a steady state, as their multiplication factors (ie, $E_{TR1} \cdot \cos\alpha_1$, $E_{TR2} \cdot \cos\alpha_2$, or $E_{TR} \cdot \cos\alpha$) are less than 1 when angles (ie, α_1, α_2, or α) are between 0° and 90°. This steady state was verified by simulating the two equations with the following imaging conditions: $TR/TR_1/TR_2$ = 3000/12/2988 ms, T_1 = 1.5 seconds, α_1 = 10°, and flip angle for the main EPI readout (α and α_2) with three different angles (90°, 60°, and 45°). Here, the time required for single-slice encoding was kept identical for both the standard and TR-external schemes (ie, $TR = TR_1 + TR_2$). In the TR-external scheme, TR_1 was kept as short as possible while still being able to accommodate all necessary imaging components (eg, RF or imaging gradients); 12 ms was enough to support the low-resolution (2.50×2.50 mm^2) as well as the high-resolution fMRI (0.73×0.73 mm^2) performed in the present study. Under the condition that TR_1 is relatively short, the flip angle (α_1) also needs to be small to avoid strong signal saturation in the next main EPI readout loop. For that reason, α_1 was set to 10° here.

The steady state was further verified with data from a healthy subject obtained with the following imaging conditions: FOV = 210×210 mm^2, matrix size = 84×84 (2.50×2.50 mm^2), 32 slices with 2.5-mm thickness and the same TR and flip-angle settings as the simulation. In this work, all in vivo measurements were performed with healthy volunteers, with no medical conditions or neurological illnesses. After a complete description of the study, written informed consent was obtained before scanning. The local institutional review board (RWTH Aachen University, Germany) approved the study protocol, screening questionnaires, and consent forms. All experiments were carried out at 3 T (Trio/Prisma, Siemens, Germany).

2.3 | Optimal flip angle for the TR-external scheme

As previously mentioned, a small angle of α_1 in the TR-external scheme does not lead to a significant saturation of longitudinal magnetization in the main EPI readout loop. However, the small angle can result in low SNR for navigator echoes, which could degrade the performance of EPI ghost correction. Here, an optimal flip angle for navigator echoes was determined by the strength of steady-state level of the main EPI loop and the performance of ghost artifact removal. For this purpose, in vivo data were acquired with the following range of α_1: 1°, 2°, …, 10°, 12°, 14°, …, 20°. The other imaging parameters were the same as the previous in vivo measurements, except that α and α_2 were fixed as 90° here. Data were acquired with both standard and TR-external schemes.

The performance of ghost artifact removal was quantitatively inspected by computing the remaining ghost signals. For this purpose, the ghost mask of each slice was defined by the following procedure. Initially, the ghost region was estimated by shifting the brain mask by FOV/2 and –FOV/2. This initial estimation was then further restricted to exclude the voxels within the brain mask, resulting in two ghost regions for every slice: one over the brain mask and the other one under the brain mask. Here, the mean ghost signal within the ghost mask was calculated for each α_1.

2.4 | Evaluation of reconstructed images and SNR

For the determined optimal flip angle, the performance of the TR-external scheme was evaluated in terms of the reconstructed image quality, image SNR, and temporal SNR (tSNR). The low-resolution protocol (2.50×2.50 mm^2) used in the previous in vivo measurement, was measured for 50 temporal volumes using both the standard and the TR-external scheme. To reduce motion effects that might exist during the scan, time-series data, realigned by *SPM12* (Wellcome Department of Imaging Neuroscience, University College London, London, United Kingdom), were used in this analysis. For the calculation of image SNR and tSNR, three regions of interest (ROIs) were defined: one for the signal region ("signal") and the other two for the background region. The two ROIs in the background region are the area where ghost artifacts may exist ("background: ghost") and the rest of the background area ("background: other"). The image SNR was obtained by computing the ratio of the signal average of the "signal" region to the signal SD of the "background: other" region. The tSNR calculation was carried out for all three ROIs, and the mean ± SD

value within each ROI was obtained. Here, the similarity of tSNR between the two schemes was further verified by inspecting the histogram distribution of the tSNR values.

The performance evaluation was further carried out with a submillimeter-resolution protocol. Both the standard and the TR-external schemes were optimized to offer the maximum possible matrix size for the given condition: TR/TE = 3000/35 ms and FOV = 210 × 210 mm^2, slice thickness = 2.3 mm, partial Fourier = 5/8, 2-fold in-plane (parallel imaging), and 3-fold interplane (multiband) acceleration. The missing lines in the partial k-space data were estimated using a phase-correction method that is denoted as the "Submatrix" method in the Siemens system.[15] As a result, the matrix achieved by the standard and the TR-external scheme was 256 × 256 (0.82 × 0.82 mm^2) and 288 × 288 (0.73 × 0.73 mm^2), respectively; the number of slices achieved was the same (48) for both schemes. The increased matrix size was a direct consequence of achieving a shorter TE in the TR-external scheme. Here, for comparison purposes, two additional protocols were used, each of which was set up with the other matrix size for each scheme. For the standard scheme, the matrix size of 288 × 288 was implemented with its shortest possible TE (41 ms). These four protocols were measured with a phantom and a healthy volunteer.

2.5 | Visual fMRI

The use of the TR-external scheme for fMRI was demonstrated with a determined optimal flip angle of 9°, as experimentally derived in the Results section. A visual checkerboard paradigm was used to elicit circumscribed activation in the visual cortex. The imaging protocol consisted of three dummy scans for reaching a steady state and 72 scans consisting of six cycles of baseline-activation states, each lasting six volume acquisitions. The total scan time for each baseline and activation block was 18 seconds (ie, 6 TR).

Three healthy volunteers participated in this fMRI study using the low-resolution protocol (2.50 × 2.50 mm^2) described previously. For comparison, the same fMRI session was also repeated with the standard scheme. Finally, the submillimeter-resolution protocol from the TR-external scheme (ie, matrix: 288 × 288; 0.73 × 0.73 mm^2) was used in the same visual fMRI paradigm, and its feasibility was demonstrated.

The fMRI data were analyzed with *SPM12*. Following preprocessing of the fMRI data (realignment, co-registration with MPRAGE, normalization to the MNI space, and spatial smoothing), first-level analysis was performed based on a general linear model. After estimating the general linear model parameters with the classical method (restricted maximum likelihood), a contrast image was obtained with a contrast vector of (−1 [baseline]; 1 [activation]). The normalization voxel size and the Gaussian kernel size for smoothing was set to the same voxel size used for each low-resolution and each high-resolution fMRI measurement. However, particularly for the high-resolution fMRI data, the co-registration and smoothing steps were excluded from the preprocessing steps. This was to prevent the possibility of an error being introduced from these steps, which might affect the spatial localization of the high-resolution functional data. Therefore, the activated voxels from high-resolution fMRI are displayed on the preprocessed EPI scan, while those from low-resolution fMRI are displayed on the MPRAGE scan. For the low-resolution fMRI data, in which two different methods were used, a fixed-effect analysis[16] was performed to inspect the effect of the different methods on the BOLD detection using the 3-subject data sets.

3 | RESULTS

3.1 | Evolution of transverse magnetization: steady state

The simulation results of the two steady-state equations are plotted in Figure 2A. Here, the signal intensities in all of the plots were normalized in relation to the first point value of the 90° plot of the standard scheme. The figure reveals that for all excitation angles, the transverse magnetization was saturated to a certain level (ie, steady state) in both the standard and the TR-external schemes. This was further verified with in vivo data, as shown in Figure 2B. The signal intensities shown in the in vivo data represent the averaged signals computed over entire slices. Visual inspection of the two subfigures suggests that the signal behavior from the in vivo data is quite similar to that from the simulation data. The signal fluctuations observed in the in vivo data were possibly due to physiological effects or subject motion during the acquisitions. Here, one of the reasons for the signal-level differences between the simulation and in vivo data was the difference of applied T_1 values: Only a single T_1 value (1.5 seconds) was considered in the simulation, whereas various T_1 values were mixed when computing the averaged signals of in vivo data.

3.2 | Optimal flip angle for the TR-external scheme

TR-external scheme data were acquired from an in vivo subject for the various α_1 angles. For each angle, the averaged signals over entire slices were computed for the volume in which the steady state had been already attained. The same procedure was repeated for the standard-scheme data. Figure 2C depicts the relative signal level of the TR-external scheme with respect to various α_1 angles; The signal level of the standard scheme was normalized to 1. As shown in this

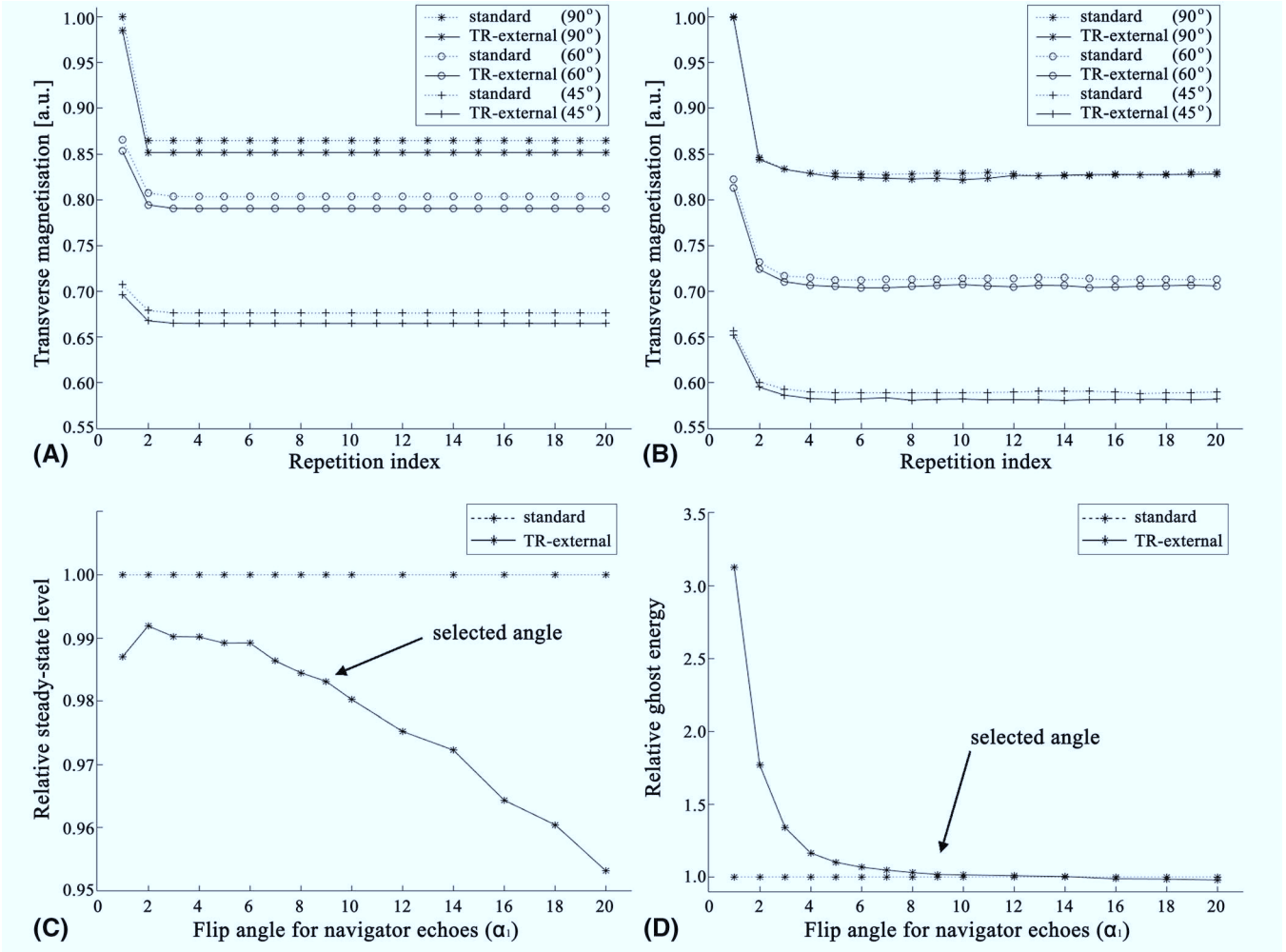

FIGURE 2 The top row shows the evolution of transverse magnetization from the simulation (A) and the in vivo data (B). The bottom row shows the performance of the TR-external scheme for the following criteria: relative strength of the steady-state level with respect to the α_1 (C) and the remaining relative mean ghost signals with respect to the α_1 (D). To aid comparison, a reference line ("standard") is depicted with a dotted line in (C) and (D)

figure, as α_1 increases, the signal level of the TR-external scheme monotonically decreases, which indicates that α_1 needs to be smaller to achieve a higher steady-state signal level. The lower signal level at the first point (α_1 of 1°) than the second point (α_1 of 2°) was primarily due to the loss of signal in the brain regions, caused by the fact that ghost artifacts were not properly removed and a large amount of ghost signals was distributed in the background region.

When the signal reaches a steady state, with the TR_1 much smaller than T_1 (ie, $TR_1 \ll T_1$), as is the case used here, Equation (1) can be further approximated to the following simpler formula:

$$M^{\text{ext}}_{xy(\text{steady})}\left(0^+\right) \approx M_{\text{eq}} \cdot \left[\frac{\left(1-E_{\text{TR2}}\right)\cdot\cos\alpha_1}{1-\left(E_{\text{TR2}}\cdot\cos\alpha_2\right)}\right]\cdot\sin\left(\alpha_2\right) \qquad (3)$$

For the standard scheme, Equation (2) can be reformulated as follows when the signal reaches a steady state:

$$M^{\text{std}}_{xy(\text{steady})}\left(0^+\right) \approx M_{\text{eq}} \cdot \left[\frac{\left(1-E_{\text{TR}}\right)}{1-\left(E_{\text{TR}}\cdot\cos\alpha\right)}\right]\cdot\sin\left(\alpha\right) \qquad (4)$$

From these two equations, it can be seen that if TR_2 and α_2 are set equal to TR and α, respectively, the transverse magnetization level of the TR-external scheme simply becomes equivalent to that of the standard scheme modulated by $\cos(\alpha_1)$. This feature can be observed in Figure 2C, which shows that the signal nearly drops according to the cosine function with respect to α_1.

Figure 2D depicts the mean ghost signals with respect to α_1. As expected, it was observed that as α_1 increases, the performance of ghost artifact removal improves (ie, the remaining mean ghost signals decreases). Here, an angle of 9° was determined to yield a steady-state signal level comparable to that of the standard scheme, while maintaining favorable performance in ghost artifact removal. For this angle, the steady-state level of the TR-external scheme was about 98% of that

of the standard scheme, and the performance of ghost removal was also quite similar between the two schemes, as shown in the figure.

3.3 | Evaluation of reconstructed images and SNR: Low-resolution

Figure 3 exhibits reconstructed images from 1 representative subject, in whom the TR-external scheme image was obtained with the angel set at 9°. Both images were taken at an identical slice position. It is observed that the TR-external scheme image was reconstructed without any noticeable ghost artifacts.

Table 1 lists the computed image SNR and tSNR obtained from the two schemes. The results reveal that for all cases (ie, image SNR and tSNR for three different ROIs), the SNR of the TR-external scheme has features that are very comparable to those of the standard scheme. Figure 4 depicts the histogram distribution of the tSNR values obtained for each ROI. Figure 4A presents the three ROIs (signal, background: ghost, and background: other) from a representative slice used in the respective analysis. The histograms obtained from the standard and the TR-external scheme are overlaid on the same plot in black and white, respectively. The overlapped regions are presented in gray. The results illustrate that for almost all ranges, the histograms from the two schemes essentially match each other.

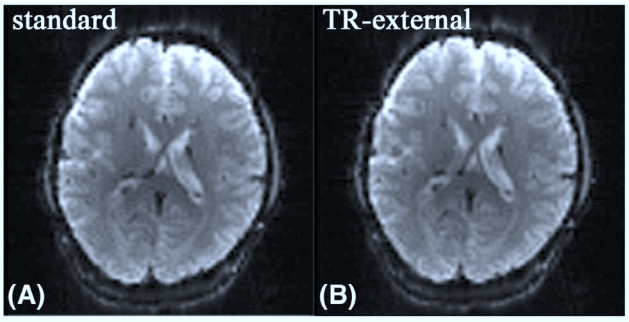

FIGURE 3 Reconstructed images (2.50×2.50 mm^2) obtained from the standard (A) and TR-external schemes (B)

3.4 | Evaluation of reconstructed images and SNR: Submillimeter resolution

Figure 5 depicts reconstructed images from the submillimeter-resolution protocols (see Table 2). Here, a representative slice was chosen from each phantom and in vivo data set. The figure reveals that all of the images are well reconstructed without significant image degradations. That is, the level of ghost or image reconstruction artifacts that might exist from the acceleration techniques is observed to be similar between the two different schemes. Visual comparison of the in vivo images with the same nominal resolution (first and second columns) suggests that the spatial resolution from the two protocols is nearly identical. This can also be readily expected by the fact that, in theory, the shape of the point spread function from the TR-external scheme is equivalent to that of the standard scheme. As a consequence, blurring artifacts are expected in both the standard and TR-external schemes to the same degree. A detailed point spread function analysis is shown in the Supporting Information.

In addition, the in vivo image from a larger matrix size (288 × 288/TE 35 ms/TR-external) depicts a slightly better spatial resolution than the lower-resolution case (256 × 256/TE 35 ms/standard). To aid visual inspection, three ROIs were selected, in which several arrows indicate the brain regions for comparison. Here, particularly for the locations marked by P_1, P_2 and P_3, horizontal line profiles were additionally examined. As shown in the figure, the TR-external scheme shows enhanced spatial resolution for the indicated brain regions, when compared with the standard scheme. This fact is further verified by the three line profiles, illustrating that the TR-external scheme has more distinct contrasts. Here, because of the use of a smaller voxel, the SNR of the TR-external scheme image (288 × 288; TE 35) is slightly lower than that of the standard scheme image (256 × 256; TE 35). However, an even lower SNR can be observed in the higher-resolution image from the standard scheme (256 × 256; TE 41), due to the use of a longer TE.

The quantitative SNR results are shown in the second (phantom) and third (in vivo) columns of Table 2. The comparison between the first and the second protocols (ie, same matrix size and same TE) shows that both the image SNR and

TABLE 1 Image SNR and tSNR results from the low-resolution protocol

	ROI	Standard	TR-external
Image SNR		78.13	77.96
tSNR	Signal	65.71 ± 35.07	64.72 ± 34.69
	Background: ghost (ghost signal ratio, %)	10.18 ± 2.60 (15.49 ± 7.41%)	10.04 ± 2.42 (15.51 ± 6.98%)
	Background: other (noise signal ratio, %)	8.02 ± 2.07 (12.21 ± 5.90%)	8.06 ± 1.99 (12.45 ± 5.74%)

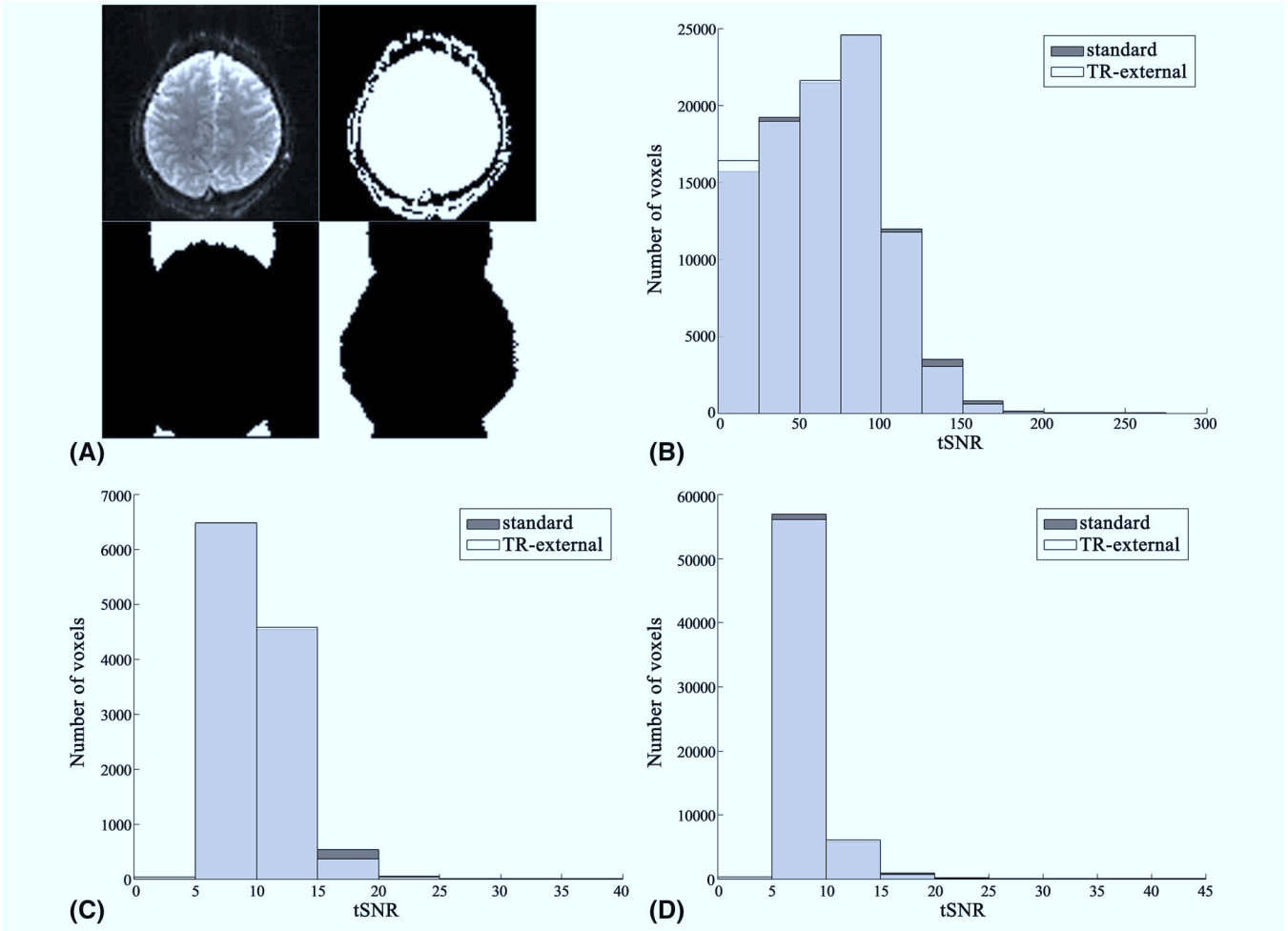

FIGURE 4 Histograms of the temporal SNR (tSNR) values. A, For a representative slice (top left), masks are shown for the "signal" (top-right), "background: ghost" (bottom-left), and "background: other" (bottom-right) regions. The histogram of the tSNR values from each region of interest (ROI) is depicted in "signal" (B), "background: ghost" (C), and "background: other" (D) ROIs. The histograms of the standard scheme (black) and the TR-external scheme (white) are overlaid on the same plot to aid comparison; the overlapped regions are presented in gray

tSNR from the two schemes are similar to each other. When compared with lower-resolution cases (first and second rows), higher-resolution protocols (third and fourth rows) show substantially reduced SNR. Here, the third protocol has even lower SNR than the fourth protocol, due to the use of a longer TE.

3.5 | Visual fMRI: Low resolution

Figure 6A,B shows the first-level analysis results of the low-resolution (2.50×2.50 mm^2) fMRI data, obtained from 1 representative subject. The activated voxels were obtained with an uncorrected P value $< .001$ (t-value > 3.73), and are displayed in three sectional views (coronal, sagittal, and axial), which are overlaid on the normalized MPRAGE scan. Visual inspection of the figure suggests that visually induced brain activations were largely detected around the visual cortex in both schemes, and the results look similar to each other. The sectional views were probed at the MNI coordinate of 13, −87, −5 (note that the functional maps from each method are displayed with the same t-value range to aid visual comparison).

Figure 6C,D shows the results of the fixed-effect analysis. Figure 6C depicts identified voxels (an uncorrected P value $< .001$), which have stronger activation when measured by the standard scheme than measured by the TR-external scheme. Figure 6D depicts the case of the reverse contrast (TR-external scheme > standard scheme).

For quantitative investigation of the fixed-effect results obtained, a statistical analysis was carried out to examine the mean ± SD t-value, maximum t-value, and number of detected voxels for the following cases: standard > baseline, TR-external > baseline, standard > TR-external, and TR-external > standard. The statistical quantities obtained are listed in Table 3. The results in the top row show that both schemes presented a comparable performance with regard to all statistical quantities. In addition, the results in the bottom row (difference between the two schemes) reveal that

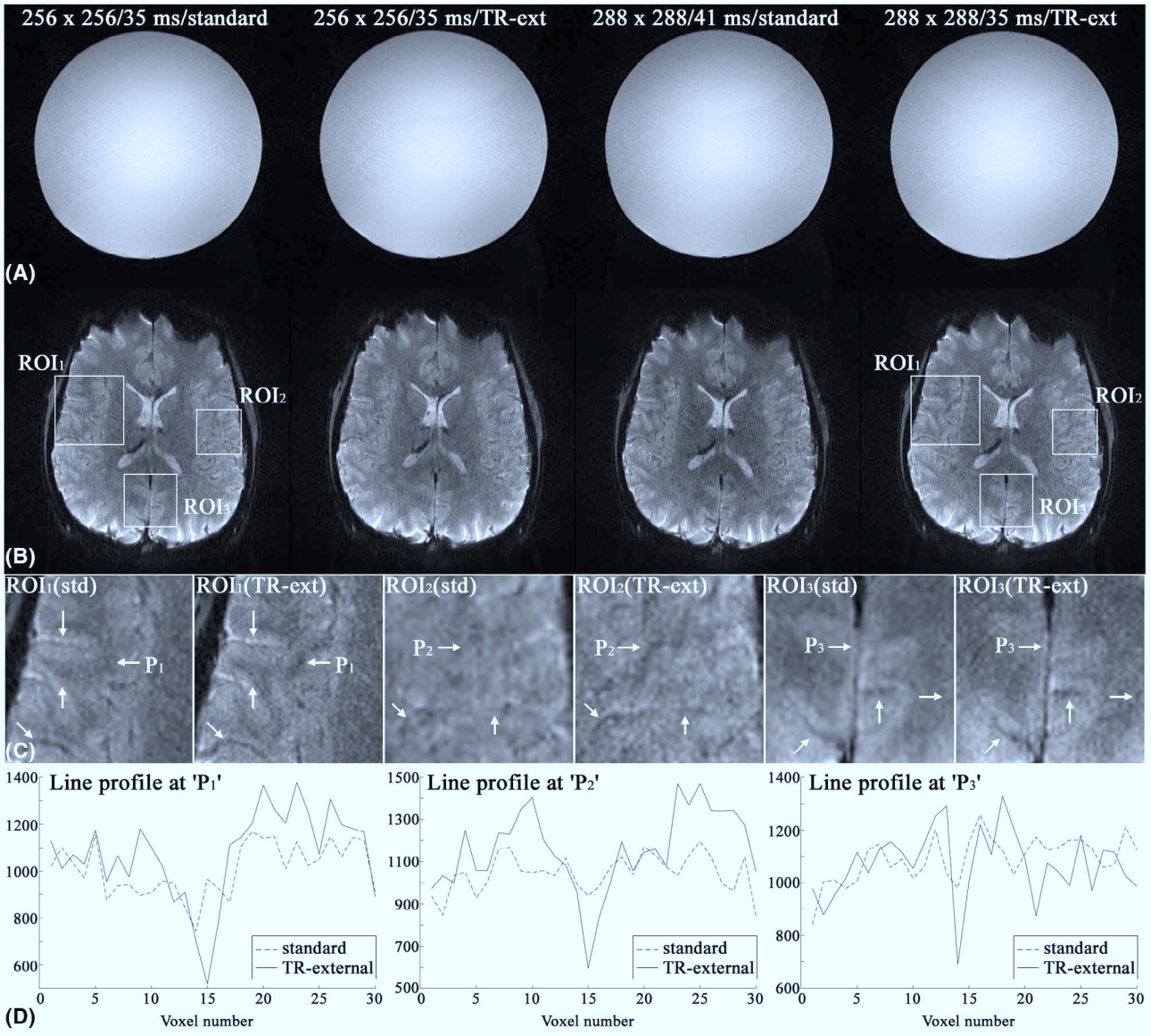

FIGURE 5 Reconstructed images of the phantom (A) and the in vivo (B) subject, acquired with the four protocols given in Table 2. Magnified brain regions for the selected three ROIs in the first and fourth column in vivo images (C), and horizontal line profiles at the indicated position (P_1, P_2, and P_3) in each ROI (D). Around the regions indicated by the arrows (see Figure C), enhanced spatial resolution can be observed in the TR-external scheme images when compared to the standard scheme images. This fact is further verified by the three line profiles, illustrating that the TR-external scheme has more distinct contrasts

TABLE 2 Image SNR and tSNR results from the submillimeter-resolution protocols

Imaging Protocols (Matrix Size/ TE/Method)	Phantom (tSNR/Image SNR)	In Vivo (tSNR/ Image SNR)
256 × 256/35 ms/standard	50.62 ± 18.91/104.43	18.04 ± 6.33/88.74
256 × 256/35 ms/TR-external	50.64 ± 18.94/104.42	18.17 ± 6.59/89.87
288 × 288/41 ms/standard	38.98 ± 14.72/90.40	15.54 ± 5.76/75.30
288 × 288/35 ms/TR-external	40.49 ± 14.93/93.70	16.76 ± 6.02/82.23

the mean and maximum *t*-values are substantially smaller than those from the top row case. Moreover, the number of detected voxels is also considerably small. These results specifically show that the performance of the TR-external scheme for the detection of BOLD signals was similar to that of the standard scheme.

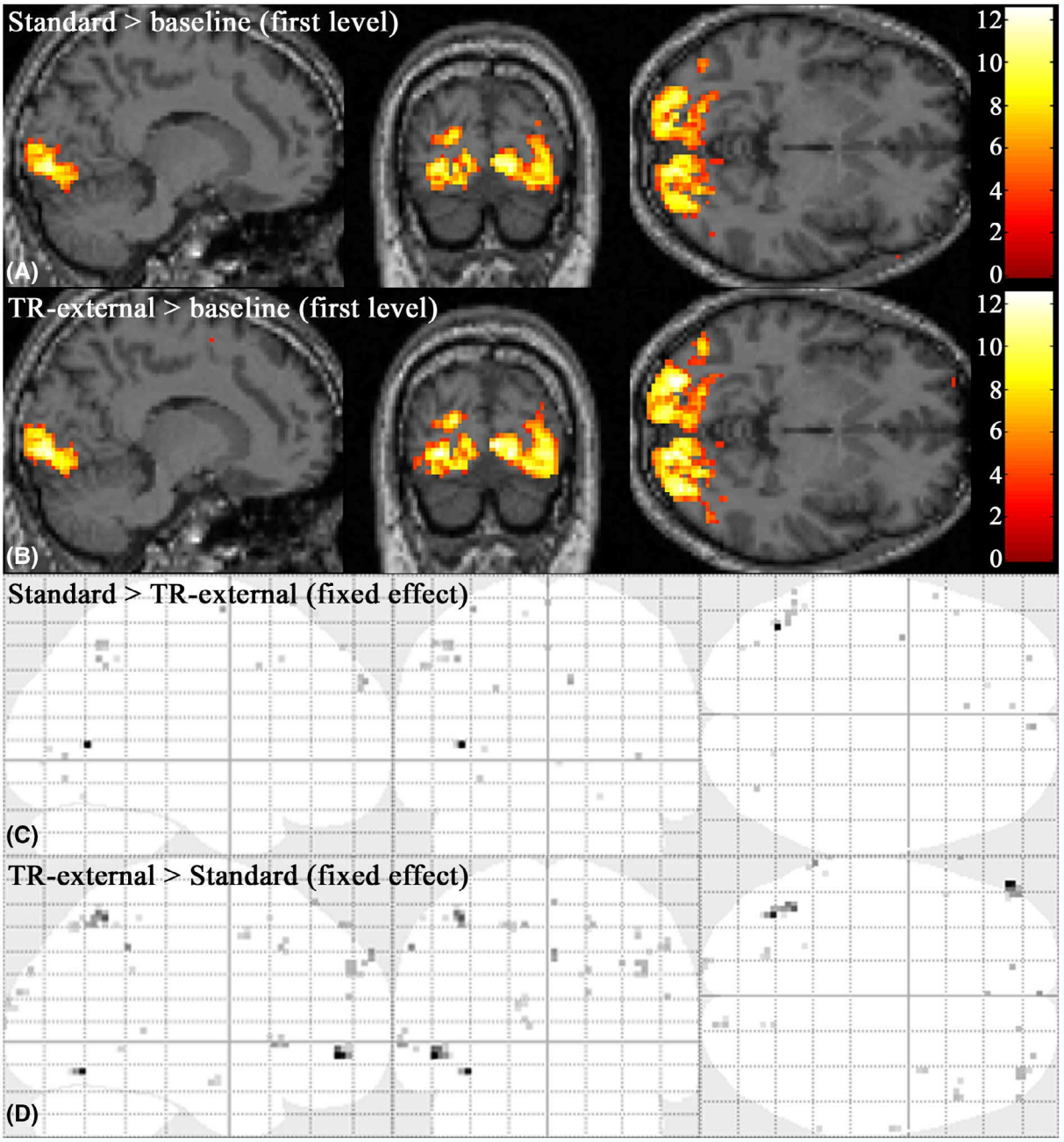

FIGURE 6 Results of low-resolution (2.50×2.50 mm^2) visual fMRI. First-level analysis results from a representative subject, obtained from the standard scheme (A) and TR-external schemes (B), where the sectional views were probed at the same MNI coordinate (x, y, z = 13, −87, −5) with the same *t*-value range. Fixed-effect results obtained for the two contrast vectors: standard scheme > TR-external scheme (C) and TR-external scheme > standard scheme (D)

TABLE 3 Examined statistical quantities for the fixed level analysis

	Mean ± SD *t*-Value	Max *t*-Value	Number of Voxels
Standard > baseline	7.02 ± 3.47	19.56	4043
TR-external > baseline	6.42 ± 3.03	19.42	4082
Standard > TR-external	3.26 ± 0.21	4.25	28
TR-external > standard	3.45 ± 0.37	5.07	85

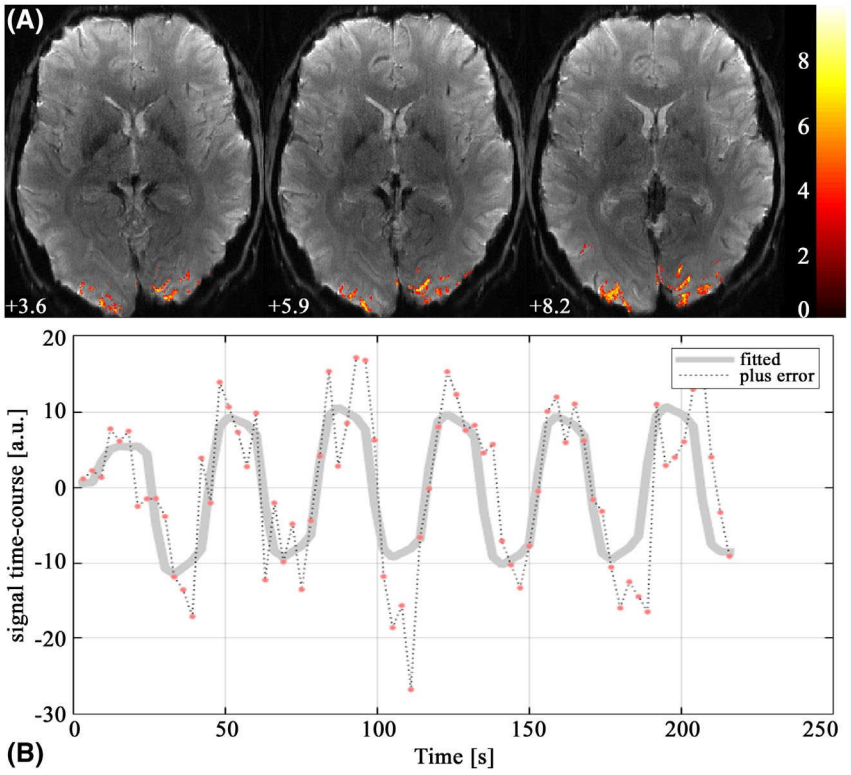

FIGURE 7 First-level analysis results of submillimeter-resolution (0.73×0.73 mm^2) fMRI. Activated voxels overlaid on the preprocessed EPI scans; three representative slices were chosen out of the entire slice set (A) and time-course data were examined at the voxel ([x, y, z] = [15.22, −94.48, 5.90]), showing the maximum *t*-score (9.69) (B). Its signal behavior shows clear hemodynamic response changes according to the designed baseline and activation blocks

3.6 | Visual fMRI: Submillimeter resolution

Functional maps obtained with the submillimeter-resolution data are shown in Figure 7A. Here, the identified activated voxels were overlaid on the preprocessed EPI scans; from the entire slice set, only three slices were chosen and displayed. The figure shows that most of the activated voxels are well localized along the cortical regions. Figure 7B shows the time-course data examined at the voxel, revealing the maximum *t*-score. Its signal behavior shows clear hemodynamic response changes according to the designed baseline and activation blocks. Here, in total, six distinct hemodynamic response lobes can be observed, which are presented in time, approximately with a given periodicity (36 seconds).

4 | DISCUSSION

In this work, a TR-external navigator acquisition scheme for EPI phase correction was implemented at 3 T, and its capability of reducing the required minimum TE was demonstrated. To assess the method, a detailed analysis of the TR-external scheme was carried out for the following points: strength of steady-state level, robustness in ghost artifact removal, and temporal stability. Here, for comparison, the same analysis was applied to the standard navigator acquisition scheme.

For the TR-external scheme, to check whether the acquisition scheme reaches steady state, and if so, how strong its level is, a mathematical equation was derived, which describes the transverse magnetization of the TR-external scheme at each repetition index. The derived equation evidently shows that the scheme reaches a steady state after a sufficient number of repetitions. In addition, the steady state was also verified with the simulation of the equation and in vivo measurements. The results revealed that the steady state was robustly achieved in the TR-external scheme, and the time required to reach the steady state (ie, required number of repetitions) was also similar to the case of the standard scheme.

When TR was given with an identical value for both methods (ie, $TR = TR_1 + TR_2$), the steady-state level of the TR-external scheme was slightly smaller than that of the standard scheme. However, the level of decrease was shown to be very small, as long as the flip angle for the navigator echoes (α_1) was kept relatively small (~10°). Therefore, a small angle is desired for α_1 to achieve a high steady-state level. However, for the effective removal of ghost artifacts, this angle needs to be large enough to generate navigator echoes with a sufficient SNR. A good compromise value, which yielded comparable performance in eliminating ghost artifacts while not leading to a substantial decrease in the steady-state level, was experimentally determined. The determined angle was 9°, and the actual in vivo images obtained with this angle exhibited features very comparable to those of the standard scheme. However, the plots in Figure 2C suggest that angles up to 20° did not induce a significant decrease in the steady-state level. Therefore, these values can be also expected to produce good results, as the steady-state level did not go below 95% of the standard scheme when the angle was 20°. This angle choice

can be determined by the scan operator and may change depending on the purpose of the study.

For the determined angle, the performance of the method was inspected by computing the image SNR and tSNR of the time-series data. Here, three different ROIs (signal, background: ghost, and background: other regions) were selected to calculate the SNR values. The results revealed that the both the image SNR and tSNR of the TR-external scheme was very comparable to that of the standard scheme. In particular, the tSNR results infer that the temporal stability of the TR-external scheme is as robust as that of the standard scheme. Moreover, the similarity of tSNR between the two schemes was further verified with the histogram plots of the tSNR values. The SNR performance of the TR-external scheme was also verified with the submillimeter-resolution protocols.

Use of the TR-external scheme for fMRI was demonstrated with a block-based visual stimulus paradigm. Here, for performance evaluation in terms of detecting BOLD signals, the low-resolution protocol (2.50×2.50 mm^2) was applied to both the standard and the TR-external schemes. The results of a 3-subject study (fixed analysis) suggest that the TR-external scheme has a nearly identical performance as the standard scheme in identifying the activated voxels. Finally, the capability of the TR-external scheme (ie, reduction of required minimum TE) was demonstrated with submillimeter-resolution (0.73×0.73 mm^2) fMRI. The functional results showed that the activated voxels are well localized along the cortical regions.

In the high-resolution study, the gain in the reduction of required minimum TE was 5.94 ms when compared with the standard scheme. This gain becomes more significant at ultrahigh-field fMRI, as a shorter TE is demanded for BOLD-based investigations due to faster T_2/T_2^* decay. As a consequence, in the standard EPI scheme, it may be necessary to sacrifice the image resolution to attain the required shorter TE. However, with the TR-external scheme, it may be even possible to perform ultrahigh-field fMRI without substantial cost to other imaging parameters. The change in T_1, as a function of field strength, may have an effect on the performance of the TR-external scheme at a different field strength. However, Equations (3) and (4) reveal that the effect of the T_1 change is expected to accrue equally for both schemes, and the ratio of the transverse-magnetization level of the TR-external scheme to that of the standard scheme (ie, $\cos[\alpha_1]$) remains the same at an arbitrary T_1 value for a typical case ($TR_1 \ll T_1$).

As mentioned previously, the gain in the TE reduction was 5.94 ms for the matrix size of 288×288. This gain is expected to increase as the matrix size becomes larger for an even higher nominal spatial resolution. This is due to the fact that a larger matrix size usually demands a longer readout duration, which directly leads to an increase in the total length of the navigator echo readout. Therefore, in those high-resolution studies, the TR-external scheme can substantially alleviate the technical limitations caused by a certain TE constraint. On the contrary, when the same TE (35 ms) is given, the maximum matrix size that could be achieved by the standard scheme was smaller (256×256; 0.82×0.82 mm^2). Therefore, in comparison, the number of voxels provided by the TR-external scheme was 26.56% larger compared with that of the standard scheme. The larger matrix size in the TR-external scheme (288×288; 0.73×0.73 mm^2) was a direct consequence of achieving a shorter TE.

As a drawback, to acquire the navigator echoes, the TR-external scheme requires an additional excitation loop (TR_1) before every main excitation loop (TR_2). This additional TR loop increases the scanning time for each slice encoding. For the case of submillimeter-resolution fMRI, in which the matrix size was 288×288, the effective increase of scanning time per slice was approximately 6 ms (ie, 12 ms [TR_1]–5.94 ms, amount of TE reduction). Nevertheless, this increase was small; thus, the number of slices achieved by the TR-external scheme protocol (matrix: 288×288; TE: 35 ms) was the same as that of the standard scheme protocol (matrix: 288×288; TE: 41 ms). When TE was identically set as 41 ms for both methods, the number of slices achieved by the TR-external scheme was only one less.

For the suppression of fat signals, a well-known technique, the chemical shift selective (CHESS) module, was used in both schemes. This CHESS module is applied before every slice encoding; hence, the required minimum TR for every slice is slightly increased. For the TR-external scheme, the CHESS module is applied before the navigator echo loop. As shown previously, the required scan time for the navigator echo loop is relatively short (ie, 12 ms). Therefore, considering the typical T_1 value of fat at 3 T (~371 ms),[17] it is expected that the effect of CHESS remains effective for the following main EPI readout loop; the longitudinal recovery of fat for the 12 ms is only 3.18%. The effective elimination of fat signals with this approach has been verified by the low-resolution (Figure 3) and high-resolution images (Figure 6 and Supporting Information Figure S1) in this work.

In the TR-external scheme, the use of an additional flip angle (α_1) leads to an increase in the used RF energy. However, when the angle was 9°, this increase was only 1% compared with the level of the standard scheme, which is quite negligible in terms of the specific absorption rate (SAR) issue. Considering the fact that the SAR of EPI sequences is generally relatively low due to its acquisition of multiple phase-encoding lines per excitation, the 1% increase in SAR is expected to have very little effect on the experimental setting of fMRI. This fact suggests that the TR-external scheme can be used at ultrahigh fields without a significant SAR concern. Here, it is also important to note that at the cost of a 1% increase in SAR, the number of voxels achieved

with the TR-external scheme was 26.56% bigger than with the standard scheme. In the Supporting Information, the performance of the TR-external scheme is assessed in more detail with the following quantitative criteria: TE reduction and scan-time increase per slice depending on the SAR level (see Supporting Information Table S1). Here, the statistical quantities were obtained for various spatial resolutions using both methods.

In this work, the TR-external scheme was used in submillimeter-resolution fMRI to reduce the required minimum TE. However, not only for high-resolution fMRI, but also for other dynamic EPI applications such as diffusion MRI, in which the TE is no longer dictated by BOLD considerations, the TR-external scheme can be effectively deployed, as EPI with a short TE is often demanded to achieve an enhanced SNR or to satisfy special constraints of the applications. Therefore, it is expected that any type of EPI application should profit from the reduced minimum TE required of the TR-external EPI phase-correction scheme.

5 | CONCLUSIONS

In this work, a TR-external navigator acquisition scheme for EPI phase correction was implemented at 3 T, and a detailed analysis of the scheme was carried out to investigate its performance. The scheme was validated with simulation and in vivo data. In the TR-external scheme, an optimal angle for the navigator echoes was experimentally determined, which yielded robust elimination of ghost artifacts with a steady-state level comparable to that of the standard navigator acquisition scheme. The SNR performance has also been shown to be similar between the two schemes, for both the low-resolution and submillimeter-resolution protocols. The use of the TR-external scheme for fMRI was demonstrated with visual fMRI. The results suggest that the performance of BOLD detection was nearly similar for both schemes. Finally, the capability of the TR-external scheme in reducing the required minimum TE was demonstrated with submillimeter-resolution fMRI, which showed that activated voxels are well localized onto the cortical ribbon.

ACKNOWLEDGMENTS

For this work, Seong Dae Yun and N. Jon Shah were funded in part internally and in part externally by the International Research Training Group (IRTG 2150)—The Neuroscience of Modulating Aggression and Impulsivity in Psychopathology (http://www.irtg2150.rwth-aachen.de/). The funders had no role in the study design, data collection and analysis, decision to publish, or preparation of the manuscript. Except for the funding sources declared here, there was no additional external funding received for this study.

ORCID

Seong Dae Yun https://orcid.org/0000-0001-7398-1899
N. Jon Shah https://orcid.org/0000-0002-8151-6169

TWITTER

N. Jon Shah @NJonShah1

REFERENCES

1. Heidemann RM, Ivanov D, Trampel R, et al. Isotropic submillimeter fMRI in the human brain at 7 T: combining reduced field-of-view imaging and partially parallel acquisitions. *Magn Reson Med*. 2012;68:1506–16.
2. Kemper VG, De Martino F, Vu AT, et al. Sub-millimeter T2 weighted fMRI at 7 T: comparison of 3D-GRASE and 2D SE-EPI. *Front Neurosci*. 2015;9:163.
3. Steele CJ, Anwander A, Bazin PL, et al. Human cerebellar sub-millimeter diffusion imaging reveals the motor and non-motor topography of the dentate nucleus. *Cereb Cortex*. 2017;27:4537–48.
4. Yun S, Shah NJ. Full-FOV, whole-brain, half-millimetre in-plane readout-segmented EPIK for high-resolution fMRI studies. In Proceedings of the 25th Annual Meeting of ISMRM, Honolulu, HI, 2017. Abstract 1485.
5. Olman CA, Van de Moortele PF, Schumacher JF, Guy JR, Uğurbil K, Yacoub E. Retinotopic mapping with spin echo BOLD at 7T. *Magn Reson Imaging*. 2010;28:1258–69.
6. Budde J, Shajan G, Zaitsev M, Scheffler K, Pohmann R. Functional MRI in human subjects with gradient-echo and spin-echo EPI at 9.4T. *Magn Reson Med*. 2014;74:209–18.
7. Yun S, Shah NJ. Whole-brain high in-plane resolution fMRI using accelerated EPIK for enhanced characterisation of functional areas at 3T. *PLoS One*. 2017;12:e0184759.
8. Heidemann RM, Porter DA, Anwander A, et al. Diffusion imaging in humans at 7T using readout-segmented EPI and GRAPPA. *Magn Reson Med*. 2010;64:9–14.
9. Glover GH, Law CS. Spiral-in/out BOLD fMRI for increased SNR and reduced susceptibility artifacts. *Magn Reson Med*. 2001;46:515–22.
10. Wielopolski PA, Schmitt F, Stehling MK. Echo-planar imaging pulse sequences. In: Schmitt F, Stehling MK, Turner R, eds. *Echo-Planar Imaging Theory, Technique and Application*. Springer-Verlag Berlin Heidelberg; 1998:96.
11. Heid O. Robust EPI phase correction. In Proceedings of the 5th Annual Meeting of ISMRM, Vancouver, British Columbia, Canada, 1997. p 2014.
12. Yun S, Shah NJ. On the analysis of EPI phase correction with small tip angle excitation to reduce minimum required TE: application to whole-Brain submillimetre resolution fMRI at 3T. In Proceedings of the 26th Annual Meeting of ISMRM, Paris, France, 2018. Abstract 4245.
13. Cheng YN, Haacke EM. Short-TR, spoiled, gradient echo imaging. *Curr Protoc Magn Reson Imaging*. 2001. doi:10.1002/0471142719.mib0501s00.
14. Gescheidtova E, Bartusek K. Longitudinal relaxation time measurement in MR with transient-state magnetization. *PIERS Online*. 2008;4:61–4.
15. Pauly J. *Partial k-Space Reconstruction*. https://users.fmrib.ox.ac.uk/~karla/reading_group/lecture_notes/Recon_Pauly_read.pdf. Accessed February 11, 2020.

16. Soleymani M, Hossein-Zadeh GA, Soltanian-Zadeh H. Fixed and random effect analysis of multi-subject fMRI data using wavelet transform. *J Neurosci Methods*. 2009;176:237–45.
17. Del Grande F, Santini F, Herzka DA, et al. Fat-suppression techniques for 3-T MR imaging of the musculoskeletal system. *Radiographics*. 2014;34:217–33.

SUPPORTING INFORMATION

Additional Supporting Information may be found online in the Supporting Information section.

FIGURE S1 A, Signal decay trajectories of the standard and TR-external schemes, simulated as a function of the phase encoding index, B, magnitude PSFs of the signal decay trajectories and C, the magnified PSFs for the selected region marked by a rectangle in (B), showing that the FWHM of the TR-external scheme is narrower than that of the standard scheme

TABLE S1 TE reduction and scan time increase per slice of the TR-external scheme when compared to the standard scheme

How to cite this article: Yun SD , Shah NJ . Analysis of EPI phase correction with low flip-angle excitation to reduce the required minimum TE: Application to whole-brain, submillimeter-resolution FMRI at 3 T. *Magn Reson Med*. 2020;84:1416–1429. https://doi.org/10.1002/mrm.28218